

1 **Impacts of an aerosol layer on a mid-latitude continental system of cumulus clouds:**
2 **how do these impacts depend on the vertical location of the aerosol layer?**

3

4 Seoung Soo Lee^{1,2}, Junshik Um^{3,4}, Won Jun Choi⁵, Kyung-Ja Ha^{2,4,6}, Chang Hoon Jung⁷,
5 Jianping Guo⁸, Youtong Zheng⁹

6

7 ¹Earth System Science Interdisciplinary Center, University of Maryland, Maryland, USA

8 ²Research Center for Climate Sciences, Pusan National University, Busan, Republic of

9 Korea

10 ³Department of Atmospheric Sciences, Pusan National University, Busan, Republic of

11 Korea

12 ⁴BK21 School of Earth and Environmental Systems, Pusan National University, Busan,

13 Republic of Korea

14 ⁵National Institute of Environmental Research, Incheon, Republic of Korea

15 ⁶Center for Climate Physics, Institute for Basic Science, Busan, Republic of Korea

16 ⁷Department of Health Management, Kyungin Women's University, Incheon, Republic of

17 Korea

18 ⁸State Key Laboratory of Severe Weather, Chinese Academy of Meteorological Sciences,

19 Beijing, China

20 ⁹The Program in Atmospheric and Oceanic Sciences, Princeton University, Princeton,

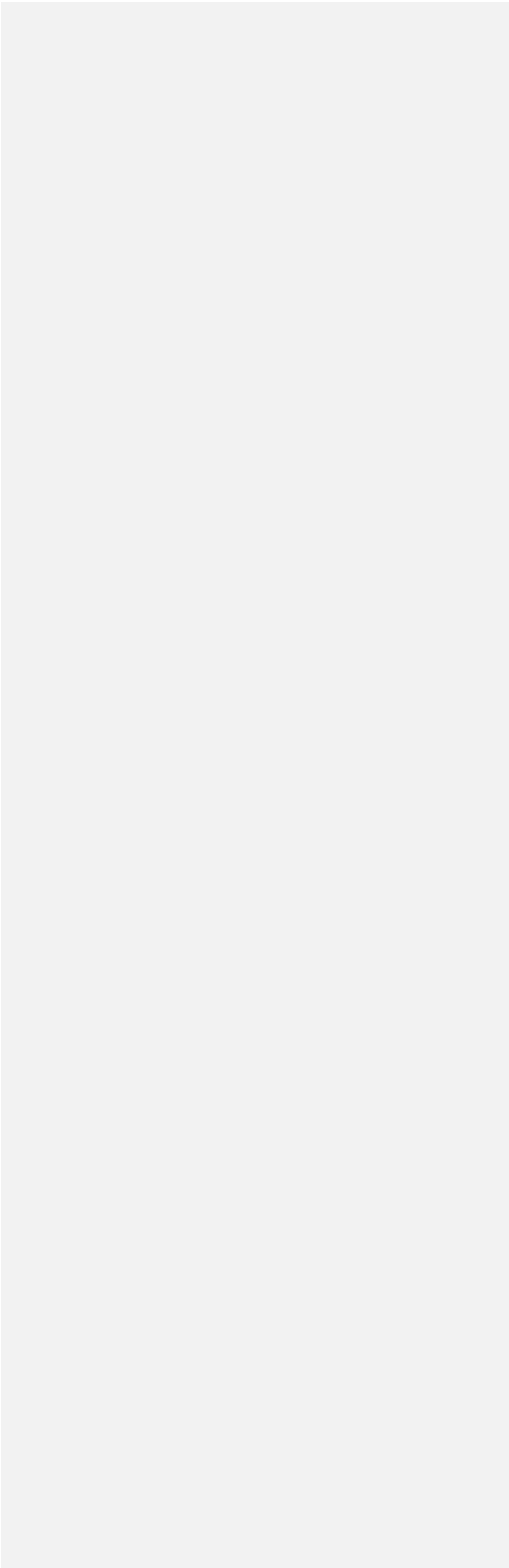
21 New Jersey, USA

22

23

24

25 Corresponding authors: Seoung Soo Lee and Junshik Um
26 E-mail: cumulss@gmail.com, slee1247@umd.edu, jjunum@pusan.ac.kr
27
28
29
30
31
32
33
34
35
36
37
38
39
40
41
42
43
44
45
46
47
48
49
50
51



52 Abstract

53

54 Effects of an aerosol layer on warm cumulus clouds in the Korean Peninsula when the layer

55 is above or around the cloud tops in the free atmosphere are compared to those effects when

56 the layer is around or below the cloud bases in the planetary boundary layer (PBL). For

57 this comparison, simulations are performed using the large-eddy simulation framework.

58 When the aerosol layer is in the PBL, aerosols absorb solar radiation and radiatively heat

59 up air enough to induce greater instability, stronger updrafts and more cloud mass than

60 when the layer is in the free atmosphere. Hence, there is a variation of cloud mass with the

61 location (or altitude) of the aerosol layer. It is found that this variation of cloud mass

62 reduces, as aerosol concentrations in the layer decrease or aerosol impacts on radiation are

63 absent. The transportation of aerosols by updrafts reduces aerosol concentrations in the

64 PBL. This in turn reduces the aerosol radiative heating, updraft intensity and cloud mass.

65

66

67

68

69

70

71

72

73

74

75

76

77

78

79

80

81

82

Deleted: upper

Deleted: low atmosphere

Deleted: low atmosphere

Deleted: upper

Deleted: the

Deleted: low atmosphere

89 1. Introduction

90

91 Warm cumulus clouds play an important role in global hydrologic and energy circulations
 92 (Warren et al., 1986; Stephens and Greenwald, 1991; Hartmann et al., 1992; Hahn and
 93 Warren, 2007; Wood, 2012). Aerosols act as radiation absorbers, and they absorb solar
 94 radiation and heat up the atmosphere to change atmospheric stability. This in turn affects
 95 thermodynamics in cumulus clouds (Hansen et al., 1997). When these aerosols act as cloud
 96 condensation nuclei (CCN), they have an impact on aerosol activation and subsequent
 97 microphysical processes in cumulus clouds (Albrecht, 1989). However, these aerosol
 98 effects on warm cumulus clouds are highly uncertain and thus cause the highest uncertainty
 99 in the prediction of future climate (Ramaswamy et al., 2001; Forster et al., 2007).

100 In recent years, people have started to take interest in how aerosol layers affect clouds
 101 when these layers are above or around the tops of clouds (e.g., de Graaf et al., 2014; Xu et
 102 al., 2017). This interest is motivated by aerosol layers that are originated from biomass
 103 burning sites in the southern Africa (Mari al., 2008; Menut et al., 2018; Haslett et al., 2019;
 104 Denjean et al., 2020). These layers are lifted and transported to the southeast Atlantic (SEA)
 105 region and located above or around the top of a large layer or deck of warm cumulus and
 106 stratocumulus clouds (Roberts et al., 2009; van der Werf et al., 2010; Che et al., 2022).
 107 Note that aerosols in the transported aerosol layers contain organic and black carbon, and
 108 these aerosols act as radiation absorbers as well as CCN (Wilcox, 2010; Deaconu et al.,
 109 2019; Chaboureau et al., 2022). Reflecting the interest, to better understand roles of aerosol
 110 layers above or around cloud tops in cloud development, there were international field
 111 campaigns in the SEA such as the National Aeronautics and Space Administration
 112 ObseRvations of Aerosols above CLouds and their intEractionS (ORACLES;
 113 <https://espo.nasa.gov/oracles/content/ORACLES>), the United Kingdom Clouds and
 114 Aerosol Radiative Impacts and Forcing (CLARIFY; Redemann et al., 2021) and the French
 115 Aerosol, Radiation and Clouds in southern Africa (AEROCLO-SA; Formenti et al., 2019)
 116 campaigns.

117 Despite above-mentioned field campaigns, effects of aerosols above or around ~~tops of~~
 118 ~~warm cumulus clouds, which are induced by shallow convection,~~ have not been examined
 119 as much as those of aerosols around or below ~~bottoms of those clouds~~ (Haywood and Shine,

Deleted: cloud

Deleted:

Deleted: cloud

123 1997; Johnson et al., 2004; McFarquhar and Wang, 2006). Motivated by this, this study
 124 delves into effects of not only aerosols around or below bottoms of warm cumulus clouds
 125 but also those above or around tops of those clouds. Through this, this study aims to
 126 contribute to the more comprehensive understanding of aerosol-radiation-cloud
 127 interactions. This more comprehensive understanding in turn contributes to more general
 128 parameterizations of those interactions for climate and weather-forecast models. To fulfill
 129 the aim, this study adopts the large-eddy simulation (LES) framework and an idealized
 130 setup for the aerosol layer.

131

132 2. Case, model and simulations

133

134 2.1 LES model

135

136 The Advanced Research Weather Research and Forecasting (ARW) model is used for LES
 137 simulations in this study. The ARW adopts a 50-m resolution for the horizontal domain. In
 138 the vertical domain, the resolution coarsens with height. The resolution in the vertical
 139 domain is 20 m just above the surface and 100 m at the model top. The ARW model is a
 140 compressible model with a nonhydrostatic status. A 5th-order monotonic advection scheme
 141 is used to advect microphysical variables (Wang et al., 2009). The ARW adopts a bin
 142 scheme, which is detailed in Khain et al. (2011), to parameterize microphysics. A set of
 143 kinetic equations is solved by the bin scheme to represent size distribution functions for
 144 each class of hydrometeors and aerosols acting as cloud condensation nuclei (CCN). The
 145 hydrometeor classes are water drops, ice crystals (plate, columnar and branch types), snow
 146 aggregates, graupel and hail. There are 33 bins for each size distribution in a way that the
 147 mass of a particle m_j in the j bin is to be $m_j = 2m_{j-1}$.

148 Aerosol sinks and sources, which include aerosol advection and activation, control
 149 the evolution of aerosol size distribution at each grid point. For example, activated particles
 150 are emptied in the corresponding bins of the aerosol spectra. Aerosol mass included in
 151 hydrometeors, after activation, is moved to different classes and sizes of hydrometeors
 152 through collision-coalescence and removed from the atmosphere once hydrometeors that
 153 contain aerosols reach the surface.

Deleted: cloud

Deleted: cloud

Moved (insertion) [1]

Deleted: is used

Deleted: The length of the domain in both the east-west and north-south directions is 20 km.

Deleted: that is at ~4.5 km in altitude

160 The Rapid Radiation Transfer Model (RRTM; Mlawer et al., 1997) has been coupled
161 to the bin microphysics scheme. Aerosols before their activation can affect radiation by
162 changing the reflection, scattering, and absorption of radiation. This radiative effect of
163 aerosol is represented following Feingold et al. (2005). The internal aerosol mixture and
164 the ARW relative humidity are used to calculate the hygroscopic growth of the aerosol
165 particles as well as their optical properties. In practice, optical property calculations with
166 the consideration of the hygroscopic growth are performed offline prior to simulation and
167 stored in lookup tables. Calculations are done for the prescribed aerosol size distribution
168 and composition, and unit concentration. During model runtime, grid-point number
169 concentration and relative humidity determine the look-up table entries that specify the
170 grid-point aerosol optical properties and are fed into the RRTM to simulate the radiative
171 effect of aerosol. The effective sizes of hydrometeors are calculated in the bin scheme and
172 the calculated sizes are transferred to the RRTM to consider effects of the effective sizes
173 on radiation.

174 The presence of aerosol perturbs the radiative fluxes reaching the surface, and its
175 subsequent partitioning into sensible and latent heat fluxes (i.e., the Bowen ratio). This is
176 accounted for with the interactive Noah land surface model (Chen and Dudhia, 2001).

177

178 **2.2 Case and simulations**

179

180 **2.2.1 Case and standard simulations**

181

182 ~~As a case study, we simulate~~ an observed system of warm cumulus clouds in a domain in
183 the Korean Peninsula on April 13th, 2016. The domain is marked in Figure 1a. Figure 2
184 shows the field of the cloud reflectivity observed by the Communication, Ocean, and
185 Meteorological Satellite (COMS). This field is at 14:00 LST on April 13th, 2016 when the
186 system is around the mature stage in the domain. The ratio of the reflected radiative flux
187 by an object to the incident radiative flux on it is the reflectivity (Liou, 2002) and thus
188 unitless. In Figure 2, we see cloud cells that are elongated in the southwest-northeast
189 direction due to the southwesterly wind.

Deleted: There is

191 The ~~simulation is performed~~ for a period between 10:00 and 18:00 LST on April 13th,
 192 2016. This period includes a time span over which the system exists. For the simulation
 193 (i.e., the control run), ~~the length of the domain in both the east-west and north-south~~
 194 ~~directions is 20 km and the model top is at ~4.5 km in altitude.~~ The time step or temporal
 195 resolution is set at 0.1 second. Initial and boundary conditions of potential temperature,
 196 specific humidity, and wind for the simulation are provided by reanalysis data. These data
 197 represent the synoptic-scale environment and are produced by the Met Office Unified
 198 Model (Brown et al., 2012) every 6 hours on a $0.11^\circ \times 0.11^\circ$ grid. Figure 3 depicts the
 199 vertical distributions of potential temperature and water-vapor mixing ratio at 09:00 LST
 200 on April 13th, 2016 in radiosonde sounding that is obtained near the domain as marked in
 201 Figure 1a. This vertical distribution represents initial environmental conditions for the
 202 control run. The conditional instability is present in the vertical profiles and this favors the
 203 development of warm cumulus clouds. An open lateral boundary condition is employed
 204 for the run. ▲

Deleted: cloud system is simulated

Moved up [1]: a 50-m resolution is used for the horizontal domain. The length of the domain in both the east-west and north-south directions is 20 km. In the vertical domain, the resolution coarsens with height. The resolution in the vertical domain is 20 m just above the surface and 100 m at the model top that is at ~4.5 km in altitude.

205 Not only a site of the aerosol robotic network (AERONET; Holben et al., 2001) but
 206 also ground stations that measure $PM_{2.5}$ are in the domain as marked in Figure 1b. The mass
 207 of aerosols with diameter smaller than $2.5 \mu\text{m}$ per unit volume of the air is $PM_{2.5}$. Around
 208 07:00 LST on April 13th, 2016, an aerosol layer advected from East Asia starts to be present
 209 in the domain. This advection of aerosols is monitored and identified by $PM_{2.5}$ which is
 210 measured by stations in the Yellow sea and domain (Eun et al., 2016; Ha et al., 2019; Lee
 211 et al., 2021). The station in the Yellow sea is marked in Figure 1a. Figure 4 shows the
 212 evolution of $PM_{2.5}$ at the station in the Yellow sea and the average $PM_{2.5}$ over stations in
 213 the domain from 03:00 LST to 18:00 LST on April 13th, 2016. Due to the aerosol-layer
 214 advection from East Asia, aerosol mass starts to increase around 04:00 LST and reaches its
 215 peak around 08:00 LST at the station in the sea. Then, in the domain, aerosol mass starts
 216 to increase around 07:00 LST, and the mass attains its peak around 11:00 LST. This depicts
 217 a situation where aerosols or an aerosol layer advected from East Asia first arrives at the
 218 station in the Yellow sea around 04:00 LST and then further advected to the east to reach
 219 the domain and to start the increase in aerosol mass there around 07:00 LST.

Formatted: Font: (Asian) Batang, (Asian) Korean

220 According to the AERONET measurement at 12:00 LST, which is ~1 hour before
 221 the observed cumulus clouds start to form, aerosol particles in the advected aerosol layer,

229 on average, are an internal mixture of 70 % ammonium sulfate, 22 % organic compound
 230 and 8% black carbon. Aerosol chemical composition in this study is assumed to be
 231 represented by this mixture in the whole domain during the whole simulation period. Based
 232 on the AERONET observation, the shape of the initial size distribution of aerosols acting
 233 as CCN is assumed to follow a bi-modal log-normal distribution as shown in Figure 5 in
 234 all parts of the domain. Modal radius of this distribution is 0.11 and 1.20 μm and standard
 235 deviation of this distribution is 1.71 and 1.92, while the partition of aerosol number, which
 236 is normalized by the total aerosol number of the size distribution, is 0.999 and 0.001 for
 237 accumulation and coarse modes, respectively. The total aerosol number concentration in
 238 the advected aerosol layer based on the AERONET-observed size distribution is ~ 15000
 239 cm^{-3} . This concentration is applied to all grid points in the aerosol layer at the first time
 240 step of the control run. This aerosol layer is idealized to be located around or below cloud
 241 bases between the surface and 1.0 km in the planetary boundary layer (PBL). Cloud bases
 242 are located around 1.0 km. At 06:00 LST, ~ 1 hour before the advected aerosol layer starts
 243 to be present, the AERONET-measured aerosol concentration is $\sim 150 \text{ cm}^{-3}$ in the domain.
 244 This aerosol concentration is assumed to be a background aerosol concentration that is not
 245 affected by the advected aerosol layer. Based on this assumption, the initial aerosol
 246 concentration is set at 150 cm^{-3} outside the layer.

247 This study compares aerosol effects on warm cumulus clouds when the aerosol layer
 248 is above or around the cloud tops to those effects when the layer is around or below the
 249 cloud bases. For this, we repeat the control run by moving the aerosol layer upward to
 250 altitudes between 2.5 and 3.5 km in the free atmosphere which is above the PBL. Here,
 251 initial aerosol concentrations in and outside the aerosol layer are 15000 cm^{-3} and 150 cm^{-3} ,
 252 respectively, in both of the runs. Altitudes between 2.5 and 3.5 km are places where cloud
 253 tops are located frequently and the simulated maximum cloud-top height is 3.3 km. This
 254 repeated run is referred to as the aro-above-cld run.

255 It is well-known that aerosol-cloud-radiation interactions are strongly dependent on
 256 aerosol concentrations (Tao et al., 2012). Hence, we want to test how results in the control
 257 and aro-above-cld runs are sensitive to aerosol concentrations in the aerosol layer. For the
 258 test, the control and aro-above-cld runs are repeated with 10 times lower initial aerosol
 259 concentrations in the aerosol layer but with no changes in initial aerosol concentrations

Deleted:

Deleted: altitudes

262 outside the layer. In these repeated runs, the aerosol concentration in the aerosol layer at
263 the first time step is 1500 cm^{-3} . Henceforth, the repeated control and aro-above-cld runs
264 are referred to as the control-1500 and aro-above-cld-1500 runs.

265

266 **2.2.2 Additional simulations**

267

268 Clouds affect aerosols through cloud processes such as nucleation of droplets and aerosol
269 transportation (or advection) by cloud-induced wind. Updrafts and downdrafts comprise
270 cloud-induced wind and transport aerosols upward and downward, respectively. Motivated
271 by this, we take interest in impacts of clouds on aerosols and how these impacts in turn
272 change the influence of aerosols on clouds. To examine this aspect of aerosol-cloud
273 interactions, the above-mentioned four standard simulations (i.e., the control, aro-above-
274 cld, control-1500 and aro-above-cld-1500 runs) are repeated. In these repeated runs,
275 aerosol concentrations at each grid point, which are set at the first time step, do not vary
276 with time or are not affected by cloud processes. These repeated runs are referred to as the
277 control-novary, aro-above-cld-novary, control-1500-novary, and aro-above-cld-1500-
278 novary runs. By comparing the standard simulations to these repeated ones, we aim to
279 identify how cloud processes affect the aerosol layer and then the impacts of the layer on
280 clouds.

281 In this study, we also aim to better understand roles of the interception (e.g., reflection,
282 scattering and absorption) of radiation by aerosols in impacts of the aerosol layer on clouds.
283 This interception of radiation by aerosols, which is referred to as aerosol radiative effects,
284 results in phenomena such as radiative heating of air by aerosols. To better understand roles
285 of aerosol radiative effects, the above four standard simulations are repeated again by
286 turning off aerosol radiative effects. These repeated runs are the control-norad, aro-above-
287 cld-norad, control-1500-norad, aro-above-cld-1500-norad runs. The summary of
288 simulations in this study is given in Table 1.

289

290 **3. Results**

291

292 **3.1 The control and aro-above-cld runs**

293

294 Figure 6 depicts the simulated field of the cloud reflectivity at 14:00 LST on April 13th,
 295 2016 in the control run. Similar to the observed counterpart in Figure 2, simulated cloud
 296 cells are elongated in the southwest-northeast direction. Also, there is a good consistency
 297 in the overall cell size and population and the overall pattern of the spatial distribution of
 298 cloud cells between the observed and simulated fields. Table 3 shows comparisons of cloud
 299 and environmental variables between observation and the control run. Observation is
 300 performed by ground stations and satellites. Note that ground stations which measure PM_{2.5}
 301 as marked in Figure 1b also measure cloud and environmental variables. Table 3 shows
 302 that differences in those variables between observation and the control run are ~10%. This
 303 and Figure 6 indicate that the control run can be considered performed reasonably well.

304 Figure 7 shows the time- and area-averaged vertical distributions of cloud-liquid mass
 305 density for the standard simulations. In Figure 7, the cloud layer is between 1.0 and 3.3 km
 306 in the control run and between 0.8 and 2.6 km in the aro-above-cld run. The time- and
 307 domain-averaged cloud-liquid mass density is 0.7 and $1.3 \times 10^{-3} \text{ g m}^{-3}$ in the control run
 308 and in the aro-above-cld run, respectively. Hence, we see that clouds are thicker with their
 309 higher tops and have greater mass in the control run than in the aro-above-cld run.

310 Figure 8a shows the time series of the domain-averaged liquid-water path, which is
 311 the vertical integral of cloud-liquid mass density, for the standard simulations. During the
 312 initial stage of the cloud development between 12:50 and 13:50 LST, the average cloud
 313 mass is slightly higher in the control run than in the aro-above-cld run. Also, the average
 314 non-zero cloud mass starts to appear earlier in the control run. Over the period between
 315 13:50 and 14:10 LST, there is a jump (or rapid increase or surge) in the average cloud mass
 316 in the control run but not in the aro-above-cld run. During this period with the jump, at
 317 some specific time points, the average mass is ~one order of magnitude higher in the
 318 control run. Of interest is that just after the jump and at 14:10 LST, the average mass in the
 319 control run starts to decrease and at 14:40 LST, becomes lower than that in the aro-above-
 320 cld run. Hence, the greater time- and domain-averaged cloud mass in the control run is
 321 mainly attributed to the jump. Figures 8b and 8c show the time series of the domain-
 322 averaged updraft speed and condensation rates, respectively. These figures indicate that the
 323 average updraft mass fluxes and associated condensation rates in the control run are also

Formatted: Superscript

Moved down [2]: Figure 6 shows the time- and area-averaged vertical distributions of cloud-liquid mass density for the standard simulations. In Figure 6, the cloud layer is between 1.0 and 3.3 km in the control run and between 0.8 and 2.6 km in the aro-above-cld run. The time- and domain-averaged cloud-liquid mass density is 0.7 and $1.3 \times 10^{-3} \text{ g m}^{-3}$ in the control run and in the aro-above-cld run, respectively. Hence, we see that clouds are thicker with their higher tops and have greater mass in the control run than in the aro-above-cld run.

Table 3 shows comparisons of cloud and environmental variables between observation and the control run. Observation is performed by ground stations and satellites. Note that ground stations which measure PM_{2.5} as marked in Figure 1b also measure cloud and environmental variables. Table 3 shows that differences in those variables between observation and the control run are ~10%.

Deleted: ¶

Deleted: We utilize satellite and ground observations to evaluate the control run. The Moderate Resolution Imaging Spectroradiometer (MODIS) is a representative sensor on board polar-orbiting satellites. The MODIS passes the domain only at 10:30 am and 1:30 pm on each day. This means that it is difficult to get reliable data, which cover the whole simulation period, from the MODIS. The COMS, which is a geostationary satellite and available in East Asia, does not provide reliable data of cloud mass. However, comparatively reliable data of cloud fraction and cloud-top height throughout the whole simulation period are obtained from the COMS. Data of cloud fraction and cloud-bottom height over the whole simulation period are collected from ground observations in the domain; note that ground stations which measure PM_{2.5} as marked in Figure 1b also measure cloud fraction and cloud-bottom height. Here, cloud fraction and cloud-bottom height in the control run are compared to those from ground observations. A comparison of cloud-top height is made in the domain between the control run and the COMS. Cloud fraction, which is averaged over all time points with non-zero cloud fraction over the whole simulation period, is 0.25 in the control run. Cloud fraction is 0.21 when it is averaged over all time points with non-zero cloud fraction that are collected from all ground stations in the domain over the whole simulation period. Cloud-bottom height, which is averaged over all air columns with non-zero cloud-bottom height over the whole simulation period, is 1.0 km in the control run. Cloud-bottom height is 1.0 km, when it is averaged over all time points with non-zero cloud-bottom height that are collected from all ground stations in the domain over the whole simulation period. The average cloud-top height over all air columns with non-zero cloud-top height over the whole simulation period is 2.8 and 2.6 km in the control run and observation, respectively. The difference in each of cloud fraction, cloud-bottom and -top heights between the control run and observations is ~10%.

Deleted: s

Deleted: means

Deleted: is

Moved (insertion) [2]

Deleted: 6

Deleted: 6

Deleted: ¶

Deleted: 7

Deleted: 7

Deleted: 7

382 slightly higher than in the aro-above-cld run for the period between 12:50 and 13:50 LST.
 383 The average updraft speed and associated condensation rates jump and thus are much
 384 higher in the control run during the period between ~13:50 and ~14:10 LST (Figures 8b
 385 and 8c). After the jump, the speed and rates decrease rapidly and become lower in the
 386 control run (Figures 8b and 8c). Condensation is the only source of cloud mass in warm
 387 cumulus clouds. Also, updrafts with higher speeds tend to produce higher condensation
 388 rates for a given environmental condition. Hence, cloud mass, condensation rate and the
 389 updraft speed are closely linked to each other. This enables cloud mass, condensation rate
 390 and the updraft speed to be similar in terms of their temporal evolution in each of the
 391 control and aro-above-cld runs (Figures 8a, 8b and 8c).

392 Figure 8d shows the time series of the domain-averaged convective available potential
 393 energy (CAPE) for the control and aro-above-cld runs. Considering that updrafts grow by
 394 consuming buoyancy energy, updraft intensity is proportional to CAPE that is the integral
 395 of the buoyancy energy in the vertical domain. Hence, the evolution of CAPE is similar to
 396 that of the updraft speed, associated condensation rates and cloud mass (Figure 8). This
 397 involves the jump not only in CAPE but also in those speed, rates and mass in the control
 398 run.

399 In Figure 8, the peaks (or the maximum values) of the domain-averaged CAPE, the
 400 updraft speed, condensation rates and cloud mass in the control run occur around 14:10
 401 LST and this occurrence is earlier than that which occurs around 14:50 LST in the aro-
 402 above-cld run. This means that the cloud system in the control run reaches its mature stage
 403 earlier. Immediately after the peak around 14:10 LST, the system enters its dissipating
 404 stage in the control run. However, the system enters its dissipating stage after 14:50 LST
 405 in the aro-above-cld run. Hence, the cloud system in the control run matures and demises
 406 faster. Stated differently, the cloud system in the control run has a shorter life cycle.

407 To find mechanisms controlling the jump in CAPE which is a main cause of the greater
 408 cloud mass in the control run, the analysis of the results is done for an initial period between
 409 10:00 LST and 13:50 LST which is immediately before the jump starts to occur. The
 410 average net shortwave fluxes at the surface are shown in Table 2 for the initial period in
 411 the control and aro-above-cld runs. Table 2 shows that during the initial period, there is a
 412 smaller amount of the surface-reaching shortwave radiation in the control run than in the

Deleted: 7

Deleted: 7

Deleted: 7

Deleted: 7

Deleted: 7

Deleted: 7

Deleted: 7

Deleted: 7

Deleted: 7

Deleted: 7

423 aro-above-cld run. The aerosol layer intercepts solar radiation and reduces the surface-
 424 reaching solar radiation. In spite of the fact that the initial depth of the aerosol layer and
 425 aerosol concentrations in the layer are identical between the runs, results here indicate that
 426 the aerosol layer in the atmosphere around or below cloud bases is more efficient in the
 427 interception of solar radiation than that in the atmosphere around or above cloud tops. Due
 428 to the less solar radiation reaching the surface, the time- and area-averaged net surface heat
 429 fluxes, which are the sum of the surface sensible and latent-heat fluxes, become lower in
 430 the control run during the initial period (Table 2). Hence, the surface fluxes favor more
 431 instability or higher CAPE and associated subsequent more intense updrafts and more
 432 cloud mass in the aro-above-cld run.

433 The vertical distributions of the time- and domain-averaged radiative heating rates are
 434 obtained for the initial period. For the initial period, the average radiative heating rate is
 435 much higher in the control run than in the aro-above-cld run particularly at altitudes
 436 between 0.0 and ~1.0 km where cloud bases are located (Figure 9a). This is associated with
 437 the fact that the aerosol layer is located at altitudes between 0.0 and 1.0 km in the control
 438 run. This more radiative heating in the PBL during the initial period results in the
 439 subsequent jump in CAPE, associated higher CAPE, more intense updrafts and more cloud
 440 mass after the initial period by outweighing the lower surface heat fluxes in the control run.
 441 The aerosol layer is located at altitudes between 2.5 and 3.5 km, hence, the average
 442 radiative heating rate is higher around those altitudes in the aro-above-cld run (Figures 9a
 443 and 9b). However, this higher radiative heating rate is in the upper part of the domain and
 444 tends to induce more stabilization of the atmosphere in the aro-above-cld run. Thus, the
 445 higher radiative heating rate in the aro-above-cld run contributes to lower CAPE, less
 446 intense updrafts and less cloud mass in the aro-above-cld run especially for the period when
 447 the jumps occur in the control run.

448

449 3.2 Comparisons between simulations with different aerosol concentrations

450

451 With the lower concentration of aerosols in the aerosol layer, there are the much more
 452 surface-reaching solar radiation and resultant higher surface fluxes in the control-1500 run
 453 than in the control run and in the aro-above-cld-1500 run than in the aro-above-cld run

Deleted: in the low atmosphere

Deleted: in the upper atmosphere

Deleted: 8

Deleted: low atmosphere

Deleted: 8

Deleted: 8

460 (Table 2). This induces higher CAPE, stronger updrafts and more condensation and cloud
 461 mass in the control-1500 run than in the control run over most of the simulation period
 462 except for the period with the jump in CAPE in the control run, and in the aro-above-cld-
 463 1500 run than in the aro-above-cld run throughout the simulation period (Figure 8). This
 464 leads to the greater time- and domain-averaged cloud mass in the control-1500 run than in
 465 the control run and in the aro-above-cld-1500 run than in the aro-above-cld run (Figure 7).
 466 Regarding the control and control-1500 runs, this is despite the fact that aerosol radiative
 467 heating in the **PBL** is higher due to higher aerosol concentrations there in the control run
 468 than in the control-1500 run (Figure 9). Regarding the aro-above-cld-1500 and the aro-
 469 above-cld runs, the greater time- and domain-averaged cloud mass is contributed by lower
 470 aerosol concentrations and less aerosol radiative heating in the **free** atmosphere in the aro-
 471 above-cld-1500 run than in the aro-above-cld run (Figure 9). Figure 7 shows that the time-
 472 and domain-averaged cloud mass in the aro-above-cld-1500 run is higher than in the
 473 control run. This is due to more solar radiation reaching the surface in the aro-above-cld-
 474 1500 run (Table 2). The higher average cloud mass in the aro-above-cld-1500 run is despite
 475 higher aerosol concentrations and more aerosol radiative heating not only in the **PBL** in the
 476 control run, but also in the **free** atmosphere in the aro-above-cld-1500 run (Figure 9). Figure
 477 7 also shows that the time- and domain-averaged cloud mass in the control-1500 run is
 478 higher than in the aro-above-cld run. This is associated with the fact that more solar
 479 radiation reaches the surface in the control-1500 run than in the aro-above-cld run (Table
 480 2). The higher average cloud mass in the control-1500 run is also associated with higher
 481 aerosol concentrations and more aerosol radiative heating not only in the **PBL** in the
 482 control-1500 run, but also in the **free** atmosphere in the aro-above-cld run (Figure 9).
 483 Similar to the situation between the control and aro-above-cld runs, there is the less
 484 surface-reaching solar radiation in the control-1500 run than in the aro-above-cld-1500 run
 485 (Table 2). In association with this, there is the less surface heat fluxes in the control-1500
 486 run. However, overall, CAPE is higher and cloud mass is greater in the control-1500 run
 487 than in the aro-above-cld-1500 run (Figures 7, 8a and 8d). This is because similar to the
 488 situation between the control and aro-above-cld runs, aerosols heat up the **PBL** more in the
 489 control-1500 run and the **free** atmosphere more in the aro-above-cld-1500 run (Figure 9c).
 490 The CAPE evolution shows that there is no jump in CAPE and thus updrafts in the control-

Deleted: 7

Deleted: 6

Deleted: low atmosphere

Deleted: 8

Deleted: upper

Deleted: 8

Deleted: 6

Deleted: low atmosphere

Deleted: upper

Deleted: 8

Deleted: 6

Deleted: low atmosphere

Deleted: upper

Deleted: 8

Deleted: 6

Deleted: 7

Deleted:

Deleted: 7

Deleted: low atmosphere

Deleted: upper

Deleted: 8

512 1500 run (Figures 8b and 8d). This mainly contributes to smaller differences in CAPE,
 513 updrafts, condensation and cloud mass between the control-1500 and aro-above-cld-1500
 514 runs than between the control and aro-above-cld runs (Figures 7 and 8).

515 In the control run, the instability or CAPE accumulates or increases rapidly to reach
 516 its peak for a period between 13:50 and 14:10 LST, while in the control-1500 run, CAPE
 517 increases gradually to reach its peak from ~12:00 LST to ~14:30 LST (Figure 8d). For a
 518 period between ~14:10 and ~14:50 LST, CAPE reduces rapidly down back to the CAPE
 519 value around ~13:50 LST in the control run. However, CAPE decreases gradually and
 520 never drops back to the CAPE value at ~12:00 LST until the end of the simulation period
 521 in the control-1500 run. This leads to the shorter life cycle or lifetime of the system in the
 522 control run than in the control-1500 run as well as in the aro-above-cld run. Accompanying
 523 this is the similar life cycle between the control-1500 and aro-above-cld-1500 runs. Here,
 524 we see that as aerosol concentration increases in the aerosol layer in the atmosphere around
 525 or below cloud bases, the time scale of the accumulation and consumption of the instability
 526 or convective energy gets shorter, leading to the shorter lifetime of the cloud system.

527 3.3 Comparisons between simulations with predicted and prescribed aerosol 528 concentrations 529

530
 531 Figure 10 shows the vertical distributions of aerosol concentrations, which are averaged
 532 over the horizontal domain and simulation period, for the standard and repeated runs with
 533 no temporal variation of aerosols. Comparisons between the control and control-novary
 534 runs and between the control-1500 and control-1500-novary runs show that due to the
 535 upward transportation of aerosols by updrafts, aerosol concentrations in the aerosol layer
 536 in the PBL reduces and those in the air above the layer increases (Figures 10a and 10c).
 537 Note that the PBL is where cloud-induced updrafts develop and grow, hence, the upward
 538 transportation of aerosols by them is dominant. This leads to the more PBL, radiative
 539 heating of air by aerosols in the control-novary run than in the control run and in the
 540 control-1500-novary run than in the control-1500 run.

541 Comparisons between the aro-above-cld and aro-above-cld-novary runs and between
 542 the aro-above-cld-1500 and aro-above-cld-1500-novary runs show that due to the

Deleted: 7

Deleted: 7

Deleted: 6

Deleted: 7

Deleted: 7

Deleted: low atmosphere

Deleted: 9

Deleted: low atmosphere

Deleted: 9

Deleted: 9

Deleted: low atmosphere

Deleted: low-atmosphere

555 transportation of aerosols by downdrafts, aerosol concentrations in the aerosol layer in the
 556 free atmosphere reduces and those in the air below the layer increases (Figures 10b and
 557 10d). Note that the free atmosphere, which includes the above-PBL atmosphere around or
 558 above cloud tops, is where cloud-induced updrafts decelerate and turn into downdrafts, and
 559 the downward transportation of aerosols by them is dominant. However, those increases in
 560 aerosol concentrations in the air below the aerosol layer mainly occur between ~1.5 and
 561 ~2.5 km, and aerosol concentrations and the associated instability in the PBL do not change
 562 significantly (Figures 10b and 10d). This leads to similar instability in the PBL and CAPE,
 563 which in turn leads to similar updrafts and cloud mass between the aro-above-cld and aro-
 564 above-cld-novary runs and between the aro-above-cld-1500 and aro-above-cld-1500-
 565 novary runs (Figure 11a).

566 Due to more radiative heating of air in the PBL, there are higher CAPE, stronger
 567 updrafts and higher cloud mass in the control-novary run than in the control run and in the
 568 control-1500-novary run than in the control-1500 run (Figure 11a). It is notable that cloud
 569 mass in the control-novary run is so large that its maximum value in the vertical profile
 570 exceeds that even in the control-1500-novary run (Figure 11a). Associated with this, there
 571 are only ~20 % changes in cloud mass between the control-1500 and control-1500-novary
 572 runs, while there are as much as ~200 % changes in cloud mass between the control and
 573 control-novary runs. This indicates that with higher aerosol concentrations in the PBL,
 574 changes in cloud mass due to the wind-induced variation of those concentrations are much
 575 larger.

576

577 3.4 Comparisons between simulations with and without aerosol radiative effects,

578

579 Figure 11b shows that with no aerosol radiative effects, differences in cloud mass due to
 580 the altitude of the aerosol layer are smaller. However, even with no aerosol radiative effects,
 581 there is higher cloud mass when the aerosol layer is in the PBL than in the free atmosphere
 582 as in the standard runs. Also, cloud mass increases when aerosol radiative effects are turned
 583 off and this increase enhances as aerosol concentrations increase (Figure 11b). Here, we
 584 see that aerosol radiative effects suppress clouds and reduce cloud mass by reducing the
 585 surface-reaching solar radiation and the surface heat fluxes. The suppression of clouds and

Deleted: upper

Deleted: 9

Deleted: 9

Deleted: upper

Deleted: low atmosphere

Deleted: 9

Deleted: 9

Deleted: low atmosphere

Deleted: 0

Deleted: low atmosphere

Deleted: 0

Deleted: 0

Deleted: low atmosphere

Deleted: and those with η
no aerosol radiative effects

Deleted: 0

Deleted: low atmosphere

Deleted: upper

Deleted: 0

605 reduction in cloud mass are greater with higher aerosol concentrations, since more aerosols
606 reduce the surface-reaching solar radiation more.

607 Note that aerosol activation mainly occurs around cloud bases in the PBL and more
608 aerosols induce more activation for a given thermodynamic condition. Hence, there are
609 more aerosol activation (or nucleation of droplets) and higher cloud droplet number
610 concentration (CDNC) when the aerosol layer is in the PBL than in the free atmosphere.
611 The averaged CDNC over grid points with non-zero CDNC and the whole simulation
612 period is 532, 57, 131 and 53 cm^{-3} in the control-norad, aro-above-cld-norad, control-1500-
613 norad and the aro-above-cld-1500-norad runs, respectively. Droplets act as a source of
614 condensation, since individual droplets provide their surface areas onto which water vapor
615 condenses. Hence, higher CDNC induces more condensation and this in turn induces
616 stronger updrafts and more cloud mass with the aerosol layer in the PBL than in the free
617 atmosphere. These effects of more aerosols, which induce more condensation and stronger
618 updrafts, are generally referred to as aerosol microphysical effects (Lee et al., 2016). The
619 differences in CDNC due to the altitude of the aerosol layer increase with increasing
620 aerosol concentrations. This leads to greater differences in condensation, associated
621 updrafts and cloud mass due to the altitude of the aerosol layer with higher aerosol
622 concentrations when there are no aerosol radiative effects (Figure 11b).

623 Here, we see that differences in cloud mass due to the altitude of the aerosol layer are
624 greater when aerosol microphysical and radiative effects work together than when aerosol
625 microphysical effects work alone (Figure 11b). Also, remember that the initial
626 concentration of aerosols in the aro-above-cld-norad run is identical to that in the aro-
627 above-cld-1500-norad run in the PBL. Due to this, CDNC, condensation and cloud mass
628 in the aro-above-cld-norad run are similar to those in the aro-above-cld-1500-norad run
629 (Figure 11b).

630

631 4. Summary and conclusions

632

633 This study examined how impacts of aerosols on warm cumulus clouds in the Korean
634 Peninsula vary with the altitude of an aerosol layer. It is found that the aerosol layer
635 intercepts the surface-reaching solar radiation more when the layer is in the PBL, which

Deleted: low atmosphere

Deleted: low atmosphere

Deleted: upper

Deleted: low atmosphere

Deleted: upper

Deleted: 0

Deleted: 0

Deleted: low atmosphere

Deleted: 0

Deleted: low atmosphere

646 ~~corresponds to the atmosphere around or below cloud bases,~~ than in the free atmosphere
 647 ~~which includes the above-PBL atmosphere around or above cloud tops.~~ With the aerosol
 648 layer in the PBL, this makes the surface heat fluxes and associated CAPE lower, which
 649 tend to make updrafts weaker and cloud mass lower. However, the layer in the PBL heats
 650 up the air there more to produce the higher CAPE and cloud mass.

Deleted: upper

Deleted: .

Deleted: low atmosphere

Deleted: low atmosphere

651 With decreasing concentrations of aerosols in the aerosol layer, there are decreases in
 652 the interception of the surface-reaching solar radiation, increases in surface heat fluxes,
 653 CAPE and cloud mass. However, the decreasing concentrations of aerosols cause the jump
 654 in CAPE to disappear when the layer is in the PBL. This makes differences in cloud mass
 655 due to the altitude of the layer reduce. When the aerosol layer is in the PBL, with increasing
 656 aerosol concentrations in the layer, the lifetime of cloud system reduces and becomes
 657 shorter than when the layer is in the free atmosphere.

Deleted: low atmosphere

Deleted: low atmosphere

Deleted: upper

658 Updrafts and downdrafts in clouds transport aerosols. In particular, for the aerosol layer
 659 in the PBL, updrafts transport aerosols in the layer to places above it. This reduces aerosol
 660 concentrations in the layer, leading to reduction in radiative heating of air by aerosols,
 661 CAPE, updrafts and cloud mass. This reduction enhances with increasing aerosol
 662 concentrations in the layer. For the aerosol layer in the free atmosphere, downdrafts
 663 transport aerosols in the layer to places below it. However, this does not affect aerosol
 664 concentrations and radiative heating of air in the PBL significantly. This in turn has
 665 negligible effects on CAPE and cloud mass.

Deleted: low atmosphere

Deleted: upper

Deleted: low atmosphere

666 Aerosol radiative effects suppress clouds and reduce cloud mass by cutting down the
 667 surface-reaching solar radiation. This suppression of clouds increases with increasing
 668 aerosol concentrations in the aerosol layer. Aerosol microphysical effects enhance cloud
 669 mass and these effects are stronger with higher aerosol concentrations. Differences in cloud
 670 mass due to the altitude of the aerosol layer are enhanced when aerosol radiative effects
 671 and aerosol microphysical effects work together as compared to when only aerosol
 672 microphysical effects are present.

673 This study shows that aerosol-induced changes in the surface fluxes and those in
 674 radiative heating of air interact with each other in terms of responses of convection and
 675 clouds to aerosols. This interaction varies with the altitude of aerosols and cloud-induced
 676 wind. In general, traditional parameterizations for warm cumulus clouds in climate and

687 weather-forecast models have not been able to consider this dependence of the interaction
688 on the altitude of aerosols, since those parameterizations do not differentiate aerosol layers
689 based on their vertical locations. In addition, the cloud-induced wind at cloud scales has
690 not been represented by those parameterizations with good confidence. So, impacts of
691 aerosol transportation by cloud-induced wind on the interaction have not been properly
692 considered in those traditional parameterizations. This suggests that the vertical locations
693 of aerosols and cloud-induced wind should be added to factors that need to be considered
694 or improved to better parameterize warm cumulus clouds and their interactions with
695 aerosols.

696

697

698

699

700

701

702

703

704

705

706

707

708

709

710

711

712

713

714

715

716

717

Deleted: ¶

Deleted: ¶

720 Code/Data source and availability

721

722 Our private computer system stores the code/data which are private and used in this study.

723 Upon approval from funding sources, the data will be opened to the public. Projects related

724 to this paper have not been finished, thus, the sources prevent the data from being open to

725 the public currently. However, if information on the data is needed, contact the

726 corresponding author Seoung Soo Lee (slee1247@umd.edu).

727

728 Author contributions

729 Essential initiative ideas are provided by SSL, JU and WJC to start this work. Simulation

730 and observation data are analyzed by SSL, JU and KJH. CHJ. JG and YZ review the results

731 and contribute to their improvement.

732

733 Competing interests

734 The authors declare that they have no conflict of interest.

735

736

737

738

739

740

741

742

743

744

745

746

747

748

749

750

751

752

753

754

755

756

757

758

759

Deleted: ¶



766 Acknowledgements

767

768 This study is supported by the National Research Foundation of Korea (NRF) grant funded
769 by the Korea government (MSIT) (No. NRF2020R1A2C1003215 and No.
770 2020R1A2C1013278) and the Korea Institute of Marine Science and Technology
771 Promotion(KIMST) funded by the Ministry of Oceans and Fisheries (20210607). This
772 study is also supported by Basic Science Research Program through the NRF funded by
773 the Ministry of Education (No. 2020R1A6A1A03044834).

774

775

776

777

778

779

780

781

782

783

784

785

786

787

788

789

790

791

792

793

794

795

796

797 **References**

798

799 Albrecht, B. A.: Aerosols, cloud microphysics, and fractional cloudiness, *Science*, 245,
800 1227-1230, 1989.

801 Brown, A., Milton, S., Cullen, M., Golding, B., Mitchell, J., and Shelly, A.: Unified
802 modeling and prediction of weather and climate: A 25-year journey, *Bull. Am*
803 *Meteorol. Soc.* 93, 1865–1877, 2012.

804 Chaboureau, J.-P., Labbouz, L., Flamant, C., and Hodzic, A.: Acceleration of the southern
805 African easterly jet driven by the radiative effect of biomass burning aerosols and its
806 impact on transport during AEROCLO-sA, *Atmos. Chem. Phys.*, 22, 8639–8658,
807 <https://doi.org/10.5194/acp-22-8639-2022>, 2022.

808 Che, H., Stier, P., Watson-Parris, D., Gordon, H., and Deaconu, L.: Source attribution of
809 cloud condensation nuclei and their impact on stratocumulus clouds and radiation in
810 the south-eastern Atlantic, *Atmos. Chem. Phys.*, 22, 10789–10807,
811 <https://doi.org/10.5194/acp-22-10789-2022>, 2022.

812 Chen, F., and Dudhia, J.: Coupling an advanced land-surface hydrology model with the
813 Penn State-NCAR MM5 modeling system. Part I: Model description and
814 implementation, *Mon. Wea. Rev.*, 129, 569–585, 2001.

815 de Graaf, M., Bellouin, N., Tilstra, L.G., Haywood, J., Stammes, P.: Aerosol direct radiative
816 effect of smoke over clouds over the southeast Atlantic Ocean from 2006 to 2009.
817 *Geophys. Res. Lett.* 41, 7723-7730, 2014.

818 Deaconu, L. T., Ferlay, N., Waquet, F., Peers, F., Thieuleux, F., and Goloub, P.: Satellite
819 inference of water vapour and above cloud aerosol combined effect on radiative
820 budget and cloud top processes in the southeastern Atlantic Ocean, *Atmos. Chem.*
821 *Phys.*, 19, 11613–11634, <https://doi.org/10.5194/acp-19-11613-2019>, 2019.

822 Denjean, C., Bourriane, T., Burnet, F., Mallet, M., Maury, N., Colomb, A., Dominutti, P.,
823 Brito, J., Dupuy, R., Sellegri, K., Schwarzenboeck, A., Flamant, C., and Knippertz, P.:
824 Overview of aerosol optical properties over southern West Africa from DACCIWA
825 aircraft measurements, *Atmos. Chem. Phys.*, 20, 4735–4756,
826 <https://doi.org/10.5194/acp-20-4735-2020>, 2020.

827 Feingold, G., H. Jiang, H., and J. Y. Harrington, J. Y.: On smoke suppression of clouds in

- 828 Amazonia, *Geophys. Res. Lett.*, 32, L02804, doi:10.1029/2004GL021369, 2005.
- 829 Forster, P., et al., Changes in atmospheric constituents and in radiative forcing, in: *Climate*
830 *change 2007: the physical science basis*, Contribution of working group I to the Fourth
831 *Assessment Report of the Intergovernmental Panel on Climate Change*, edited by
832 Solomon, S., et al., Cambridge Univ. Press, New York, 2007.
- 833 Formenti, P., B. D'Anna, C. Flamant, et al.: The Aerosols, Radiation and Clouds in
834 *Southern Africa Field Campaign in Namibia: Overview, illustrative observations, and*
835 *way forward*, *Bull. Amer. Meteor. Soc.*, 100, 1277-1298, 2019.
- 836 Hahn, C. J., and Warren, S. G.: A gridded climatology of clouds over land (1971–96) and
837 *ocean (1954–97) from surface observations worldwide*. Numeric Data Package NDP-
838 026EORNL/CDIAC-153, CDIAC, Department of Energy, Oak Ridge, TN, 2007.
- 839 Hansen, J. E., Sato, M. and Ruedy, R.: Radiative forcing and climate response, *J. Geophys.*
840 *Res.*, 102, 6831–6864, 1997.
- 841 Hartmann, D. L., Ockert-Bell, M. E., and Michelsen, M. L.: The effect of cloud type on
842 *earth's energy balance—Global analysis*, *J. Climate*, 5, 1281–1304, 1992.
- 843 Haslett, S. L., Taylor, J. W., Evans, M., Morris, E., Vogel, B., Dajuma, A., Brito, J.,
844 *Batenburg, A. M., Borrmann, S., Schneider, J., Schulz, C., Denjean, C., Bourriane,*
845 *T., Knippertz, P., Dupuy, R., Schwarzenböck, A., Sauer, D., Flamant, C., Dorsey, J.,*
846 *Crawford, I., and Coe, H.: Remote biomass burning dominates southern West African*
847 *air pollution during the monsoon*, *Atmos. Chem. Phys.*, 19, 15217–15234,
848 <https://doi.org/10.5194/acp-19-15217-2019>, 2019.
- 849 Haywood, J. M. and Shine, K. P.: Multi-spectral calculations of the radiative forcing of
850 *tropospheric sulfate and soot aerosols using a column model*, *Q. J. R. Meteorol. Soc.*,
851 123, 1907–1930, 1997.
- 852 Holben, B. N., Tanré, D., Smirnov, et al.: An emerging ground-based aerosol climatology:
853 *Aerosol optical depth from AERONET*, *J. Geophys. Res.*, 106, 12067–12097, 2001.
- 854 Johnson, B. T., Shine, K. P., and Forster, P. M.: The semi-direct aerosol effect: Impact of
855 *absorbing aerosols on marine stratocumulus*, *Q. J. R. Meteorol. Soc.*, 130, 1407– 1422,
856 2004.
- 857 Khain, A., Pokrovsky, A., Rosenfeld, D., Blahak, U., and Ryzhko, A.: The role of CCN in
858 *precipitation and hail in a mid-latitude storm as seen in simulations using a spectral*

- 859 (bin) microphysics model in a 2D dynamic frame, *Atmos. Res.*, 99, 129–146, 2011.
- 860 Lee, S. S., Guo, J. M., and Li, Z.: Delaying precipitation by air pollution over the Pearl
861 River Delta. Part II: Model simulations, *J. Geophys. Res.*, 121, 11739–11760.
- 862 Lee, S. S., Ha, K.-J., Manoj, M. G., et al.: Midlatitude mixed-phase stratocumulus
863 clouds and their interactions with aerosols: how ice processes affect microphysical,
864 dynamic, and thermodynamic development in those clouds and interactions?, *Atmos.*
865 *Phys. Chem.*, 21, 16843–16868, 2021.
- 866 Mari, C. H., Cailley, G., Corre, L., Saunois, M., Attié, J. L., Thouret, V., and Stohl, A.:
867 Tracing biomass burning plumes from the Southern Hemisphere during the AMMA
868 2006 wet season experiment, *Atmos. Chem. Phys.*, 8, 3951–3961,
869 <https://doi.org/10.5194/acp-8-3951-2008>, 2008.
- 870 McFarquhar, G. M. and Wang, H.: Effects of Aerosols on Trade Wind Cumuli over the
871 Indian Ocean: Model Simulations, *Q. J. R. Meteorol. Soc.*, 132, 821–843, 2006.
- 872 Menut, L., Flamant, C., Turquety, S., Deroubaix, A., Chazette, P., and Meynadier, R.:
873 Impact of biomass burning on pollutant surface concentrations in megacities of the
874 Gulf of Guinea, *Atmos. Chem. Phys.*, 18, 2687–2707, [https://doi.org/10.5194/acp-18-](https://doi.org/10.5194/acp-18-2687-2018)
875 [2687-2018](https://doi.org/10.5194/acp-18-2687-2018), 2018.
- 876 Mlawer, E. J., Taubman, S. J., Brown, P. D., Iacono, M. J., and Clough, S. A.: RRTM, a
877 validated correlated-k model for the longwave, *J. Geophys. Res.*, 102, 16663–1668,
878 1997.
- 879 Ramaswamy, V., et al.: Radiative forcing of climate change, in *Climate Change 2001: The*
880 *Scientific Basis*, edited by J. T. Houghton et al., 349–416, Cambridge Univ. Press,
881 New York, 2001.
- 882 Redemann, J., Wood, R., Zuidema, P., et al.: An overview of the ORACLES (ObseRvations
883 of Aerosols above CLouds and their intEractionS) project: aerosol–cloud–radiation
884 interactions in the southeast Atlantic basin, *Atmos. Chem. Phys.*, 21, 1507–1563, 2021.
- 885 Roberts, G. C. and Nenes, A.: A Continuous-Flow Streamwise Thermal-Gradient CCN
886 Chamber for Atmospheric Measurements, *Aerosol Sci. Technol.*, 39, 206–221
887 <https://doi.org/10.1080/027868290913988>, 2005.
- 888 Stephens, G. L., and Greenwald, T. J.: Observations of the Earth’s radiation budget in
889 relation to atmospheric hydrology. Part II: Cloud effects and cloud feedback. *J.*

- 890 Geophys. Res., 96, 15 325–15 340, 1991.
- 891 Tao, W.-K., Chen, J.-P., Li, Z., Wang, C., and Zhang C., Impact of aerosols on convective
892 clouds and precipitation, *Rev. Geophys.*, 50, RG2001, doi:10.1029/2011RG000369,
893 2012.
- 894 Twomey, S.: The influence of pollution on the shortwave albedo of clouds, *J. Atmos. Sci.*,
895 34, 1149-1152, 1977.
- 896 Twomey, S.: Pollution and the Planetary Albedo, *Atmos. Env.*, 8, 1251-1256, 1974.
- 897 van der Werf, G. R., Randerson, J. T., Giglio, L., Collatz, G. J., Mu, M., Kasibhatla, P. S.,
898 Morton, D. C., DeFries, R. S., Jin, Y., and van Leeuwen, T. T.: Global fire emissions
899 and the contribution of deforestation, savanna, forest, agricultural, and peat fires
900 (1997–2009), *Atmos. Chem. Phys.*, 10, 11707–11735, [https://doi.org/10.5194/acp-10-](https://doi.org/10.5194/acp-10-11707-2010)
901 11707-2010, 2010.
- 902 Wang, H., Skamarock, W. C., and Feingold, G.: Evaluation of scalar advection schemes in
903 the Advanced Research WRF model using large-eddy simulations of aerosol-cloud
904 interactions, *Mon. Wea. Rev.*, 137, 2547-2558, 2009.
- 905 Warren, S. G., Hahn, C. J., London, J., Chervin, R. M., and Jenne, R. L.: Global distribution
906 of total cloud cover and cloud types over land. NCAR Tech. Note NCAR/TN-
907 273+STR, National Center for Atmospheric Research, Boulder, CO, 29 pp. + 200
908 maps, 1986.
- 909 Wilcox, E. M.: Stratocumulus cloud thickening beneath layers of absorbing smoke aerosol,
910 *Atmos. Chem. Phys.*, 10, 11769–11777, <https://doi.org/10.5194/acp-10-11769-2010>,
911 2010.
- 912 Wood, R.: Stratocumulus clouds, *Mon. Wea. Rev.*, 140, 2373-2423, 2012.
- 913 Xu, H., Guo, J., Wang, Y., et al.: Warming effect of dust aerosols modulated by overlapping
914 clouds below, *Atmos. Env.*, 166, 2017, 393-402, 2017.
- 915
916
917
918
919
920
921
922

923 **FIGURE CAPTIONS**

924

925 Figure 1. (a) An inner rectangle in the map of the Korean Peninsula represents the
 926 simulation domain. The green represents the land area and the light blue the ocean area in
 927 the map. A black dot marks the location of a site where the radiosonde sounding is obtained
 928 and a red dot the location of the PM_{2.5} station in the Yellow sea. (b) The simulation domain
 929 is shown. The black dots mark the locations of the PM_{2.5} stations and the red dot the location
 930 of the AERONET site in the domain.

931

932 Figure 2. Spatial distribution of cloud reflectivity which is unitless and observed by the
 933 COMS at 14:00 LST April 13th, 2016 in the simulation domain. Contours are at 0.11, 0.15,
 934 0.19 and 0.25.

935

936 Figure 3. Vertical distributions of potential temperature and water-vapor mixing ratio at
 937 09:00 LST on April 13th, 2016. These distributions are obtained from radiosonde sounding
 938 near the simulation domain in Figure 1a.

939

940 Figure 4. Time series of PM_{2.5} observed at the station in the Yellow sea (blue line) and of
 941 the average PM_{2.5} over stations in the simulation domain (red line) between 03:00 LST and
 942 18:00 LST on April 13th in 2016.

943

944 Figure 5. Aerosol size distribution at the surface. N represents aerosol number
 945 concentration per unit volume of air and D represents aerosol diameter.

946

947 Figure 6. Same as Figure 2 but in the control run.

948

949 Figure 7. Vertical distributions of the time- and area-averaged cloud-liquid mass density
 950 that represents cloud mass for the standard simulations (i.e., the control, aro-above-cld,
 951 control-1500 and aro-above-cld-1500 runs).

952

953 Figure 8. Time series of the domain-averaged (a) liquid-water path, (b) updraft speed, (c)
 954 condensation rate and (d) CAPE in the standard simulations.

Deleted: 1

Deleted: 6

Deleted: 7

958 Figure 9. Vertical distributions of the time- and area-averaged radiative heating rate (a) in
959 the control and aro-above-cld runs over the initial period between 10:00 and 13:50 LST,
960 (b) in the control and aro-above-cld runs and (c) in the control-1500 and aro-above-cld-
961 1500 runs over the whole simulation period.

Deleted: 1

Deleted: 8

962
963 Figure 10. Vertical distributions of the time- and area-averaged aerosol concentrations (a)
964 in the control and control-novary runs, (b) aro-above-cld and aro-above-cld-novary runs,
965 (c) control-1500 and control-novary-1500 runs and (d) aro-above-cld-1500 and aro-above-
966 cld-novary-1500 runs.

Deleted: 9

967
968 Figure 11. Vertical distributions of the time- and area-averaged cloud-liquid mass density.
969 In (a), the control-novary, aro-above-cld-novary, control-1500-novary and aro-above-cld-
970 1500-novary runs and in (b), the control-norad, aro-above-cld-norad, control-1500-norad
971 and aro-above-cld-1500-norad runs are shown together with the standard simulations.

Deleted: 0

972

973

974

975

976

977

978

979

980

981

982

983

984

985

986

987

Deleted: 1

Simulations	Altitudes of a aerosol layer (km)	Aerosol concentrations in the aerosol layer at the first time step (cm^{-3})	Aerosol evolution	Aerosol radiative effects
Control	0 - 1	15000	Present	Present
Aro-above-cld	2.5-3.5	15000	Present	Present
Control-1500	0 - 1	1500	Present	Present
Aro-above-cld-1500	2.5-3.5	1500	Present	Present
Control-novary	0 - 1	15000	Absent	Present
Aro-above-cld-novary	2.5-3.5	15000	Absent	Present
Control-1500-novary	0 - 1	1500	Absent	Present
Aro-above-cld-1500-novary	2.5-3.5	1500	Absent	Present
Control-norad	0 - 1	15000	Present	Absent
Aro-above-cld-norad	2.5-3.5	15000	Present	Absent
Control-1500-norad	0 - 1	1500	Present	Absent
Aro-above-cld-1500-norad	2.5-3.5	1500	Present	Absent

993

994 Table 1. Summary of simulations

995

996

997

998

999

1000

1001

1002

1003

1004

1005

1006

Simulations	Net solar radiation flux reaching the surface (W m ⁻²)	Surface latent heat fluxes (W m ⁻²)	Surface sensible heat fluxes (W m ⁻²)	Surface latent heat fluxes plus surface sensible heat fluxes (W m ⁻²)
Control	293 (205)	175 (120)	22 (16)	197 (136)
Aro-above-cld	306 (217)	170 (117)	48 (33)	218 (150)
Control-1500	461	250	70	320
Aro-above-cld-1500	467	248	75	323

1007

1008 Table 2. The time- and area-averaged net solar radiation, latent heat, sensible heat and total
1009 heat (sensible plus latent heat) fluxes at the surface over the whole simulation period in the
1010 standard simulations. Numbers in the parentheses are averaged over the initial period
1011 between 10:00 and 13:50 LST for the control and aro-above-cld runs.

1012

1013

1014

1015

1016

1017

1018

1019

1020

1021

1022

1023

1024

1025

1026

1027

1028

	<u>Control run</u>	<u>Observations</u>	<u>Observation sources</u>
<u>Cloud fraction (CF)</u>	<u>0.25</u>	<u>0.21</u>	<u>Ground stations</u>
<u>Cloud-top height (CTH) (km)</u>	<u>2.8</u>	<u>2.6</u>	<u>COMS</u>
<u>Cloud-bottom height (CBH) (km)</u>	<u>1.1</u>	<u>1.0</u>	<u>Ground stations</u>
<u>Cloud optical depth (COD)</u>	<u>3.5</u>	<u>3.2</u>	<u>The Moderate Resolution Imaging Spectroradiometer (MODIS)</u>
<u>Droplet effective radius (re) (μm)</u>	<u>7.5</u>	<u>8.0</u>	<u>MODIS</u>
<u>Liquid-water path (LWP) (g m^{-2})</u>	<u>17.3</u>	<u>16.8</u>	<u>MODIS</u>
<u>The surface wind speed (WS) (m s^{-1})</u>	<u>1.8</u>	<u>1.6</u>	<u>Ground stations</u>
<u>The surface wind direction (WD) (Degree; measured clockwise from geographical north)</u>	<u>220</u>	<u>230</u>	<u>Ground stations</u>
<u>The surface air temperature (ST) (Degree Celsius)</u>	<u>16.9</u>	<u>16.7</u>	<u>Ground stations</u>

Formatted: Centered

Formatted Table

Formatted: Centered

Formatted: Centered

Formatted: Centered

Formatted: Font: (Default) Batang, (Asian) Batang

Formatted: Centered

Formatted: Centered

Formatted: Superscript

Formatted: Centered

Formatted: Superscript

Formatted: Centered

1029

1030 Table 3. The simulated and observed values of cloud and environmental variables, and the
 1031 observation sources that have been used to obtain the observed values. At each observation
 1032 time (simulation time step), CF is averaged (obtained) over ground stations (grid points) in
 1033 the domain as shown in Figure 1b and the averaged (obtained) CF is averaged over the

1034 simulation period with clouds to calculate the presented and observed (simulated) CF
1035 values. To obtain the presented values of CTH, CBH, COD, re and LWP, the observed
1036 values at observation spatial points (the simulated values in grid columns for CTH, CBH
1037 and LWP and at grid points for COD and re) in the domain are averaged over areas with
1038 non-zero values at each observation time (simulation time step) and then over the
1039 simulation period with non-zero values. To obtain the presented values of WS, WD and
1040 ST, the simulated values at grid points, which correspond to the atmosphere immediately
1041 above the surface, and each simulation time step, and the observed values at ground stations
1042 and each observation time are averaged over the domain and then over the whole
1043 simulation period.
1044
1045

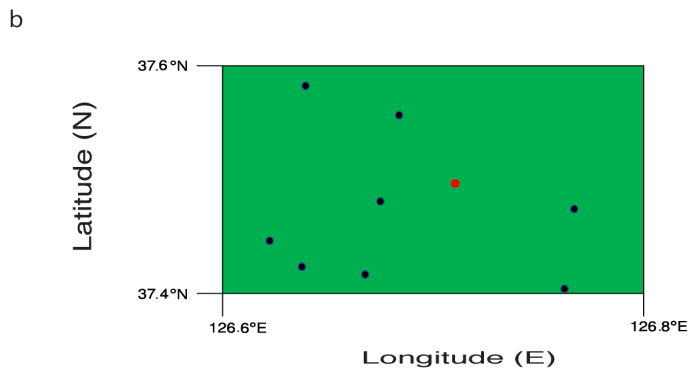
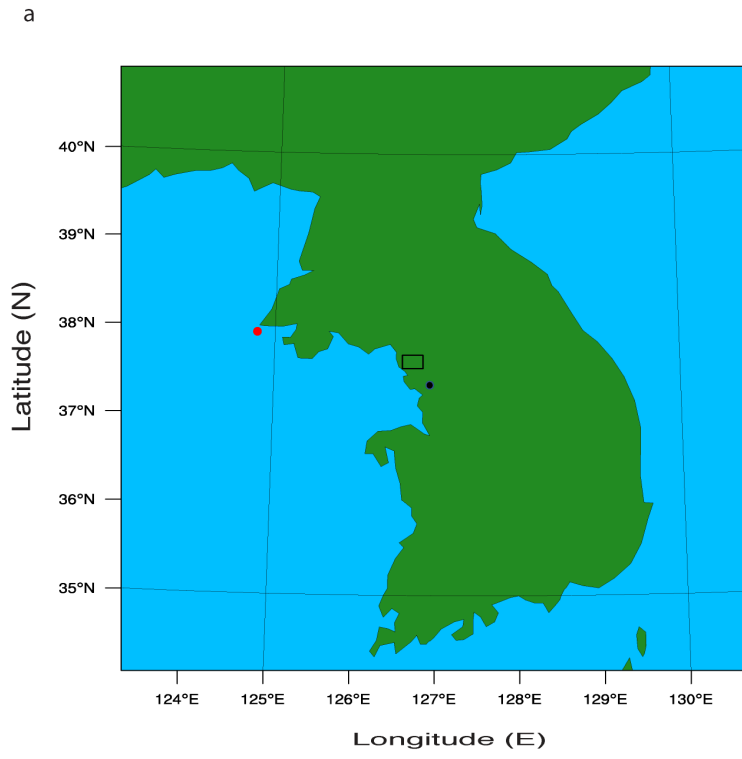
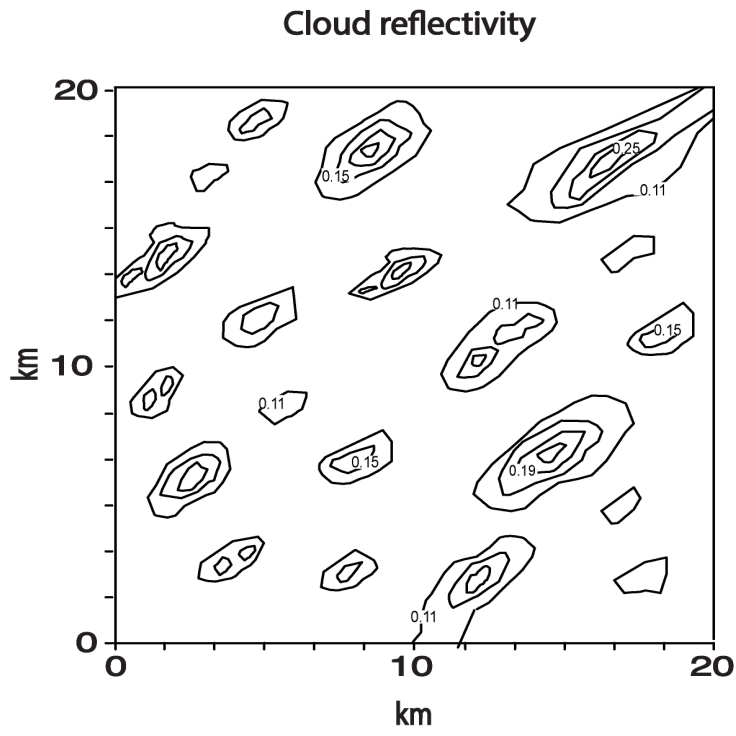


Figure 1

1046

1047

1048



1049

1050

1051

Figure 2

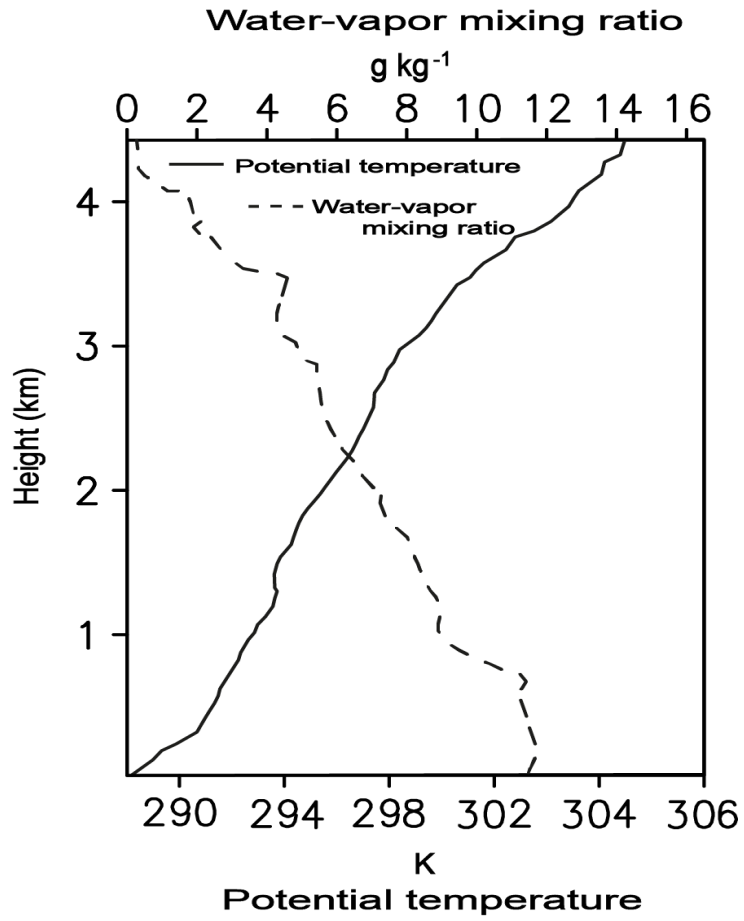


Figure 3

1052

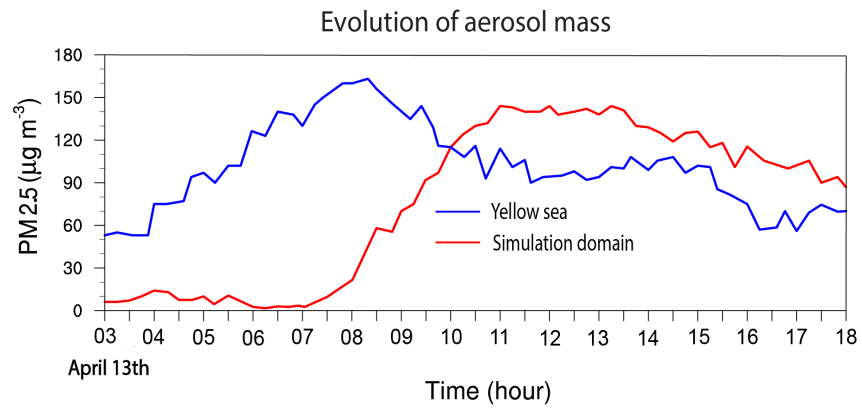
1053

1054

1055

1056

1057



1058

1059

Figure 4

1060

1061

1062

1063

1064

1065

1066

1067

1068

1069

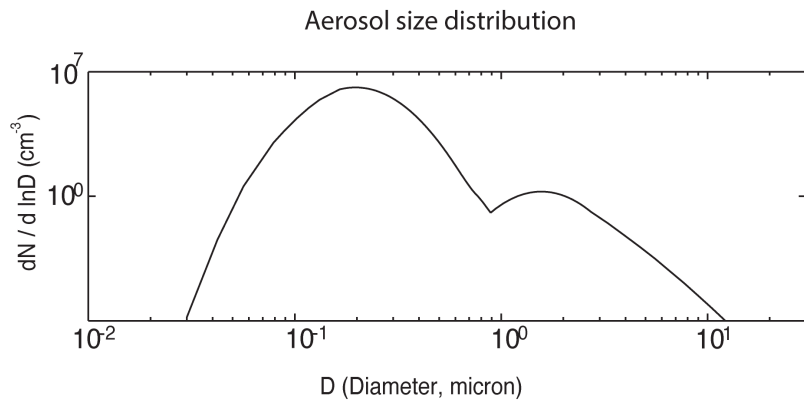
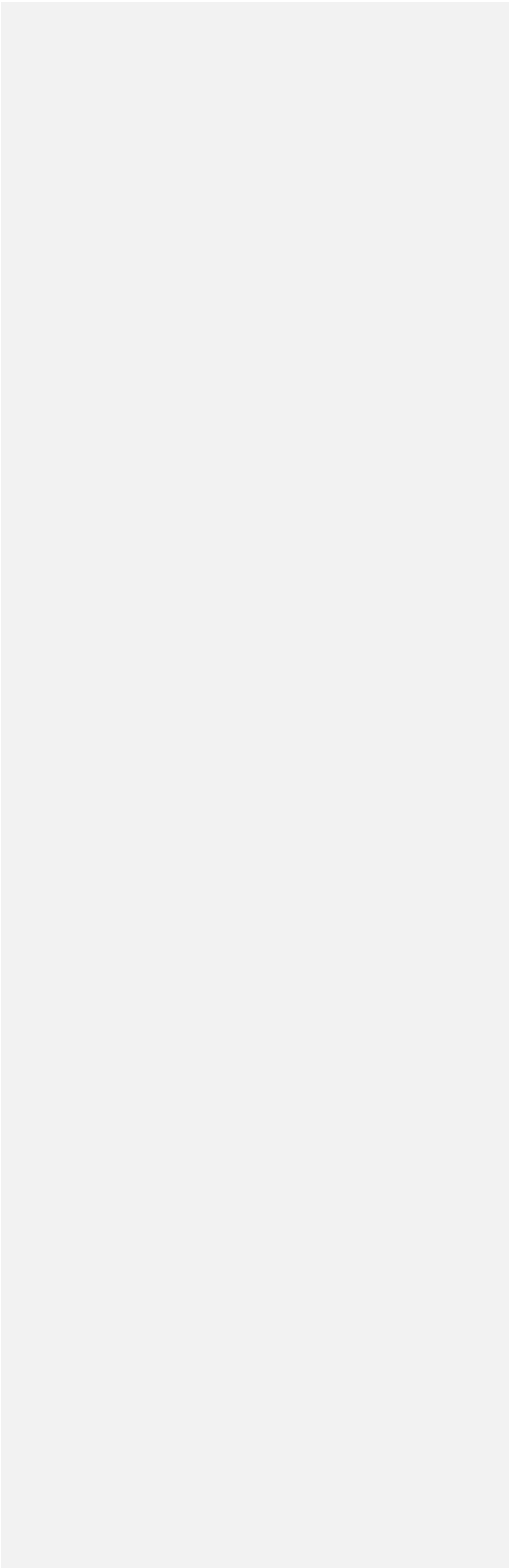
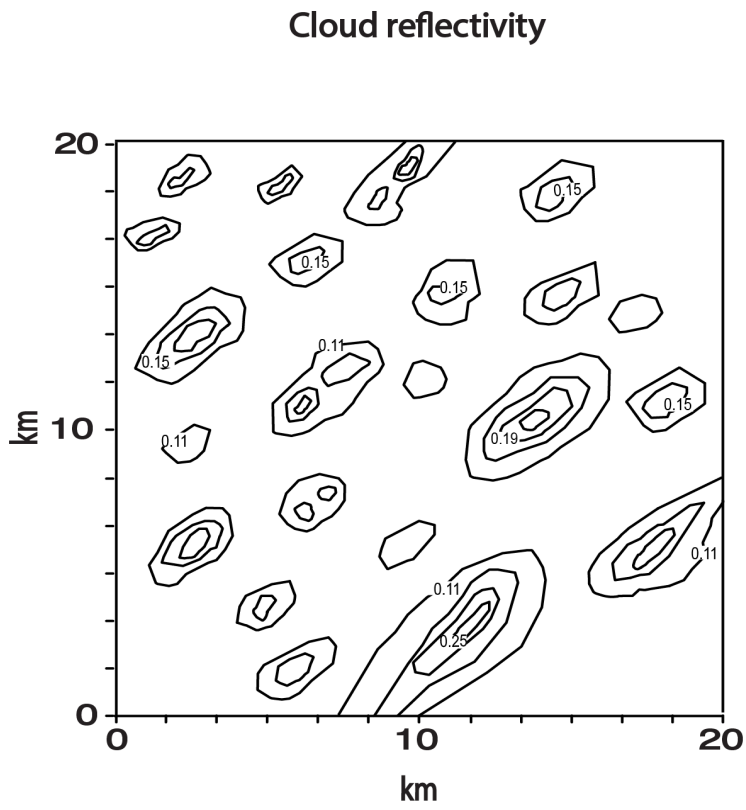


Figure 5

1070
1071
1072
1073
1074
1075
1076
1077
1078
1079
1080
1081
1082





1083

1084

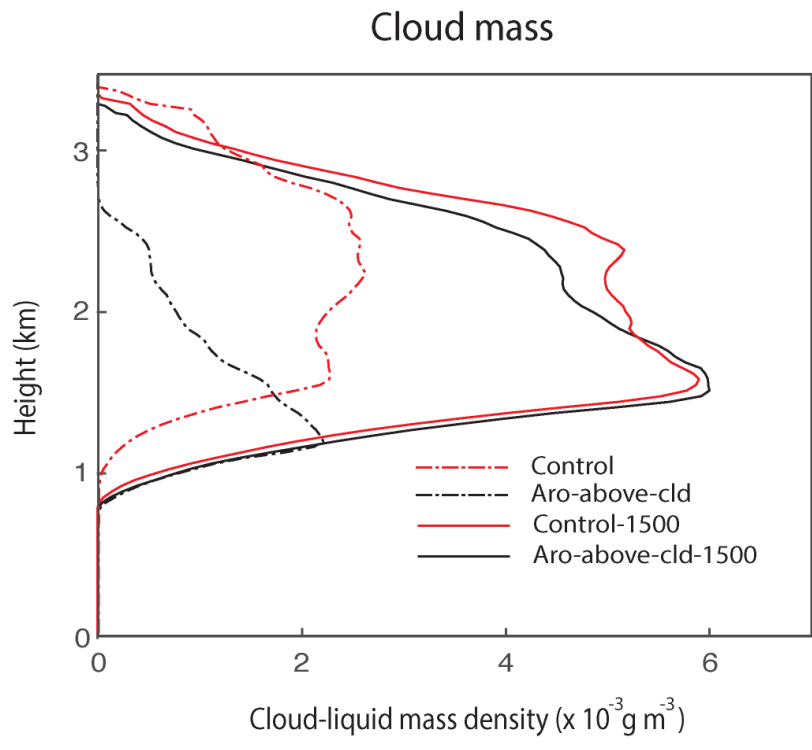
1085

1086

1087

1088

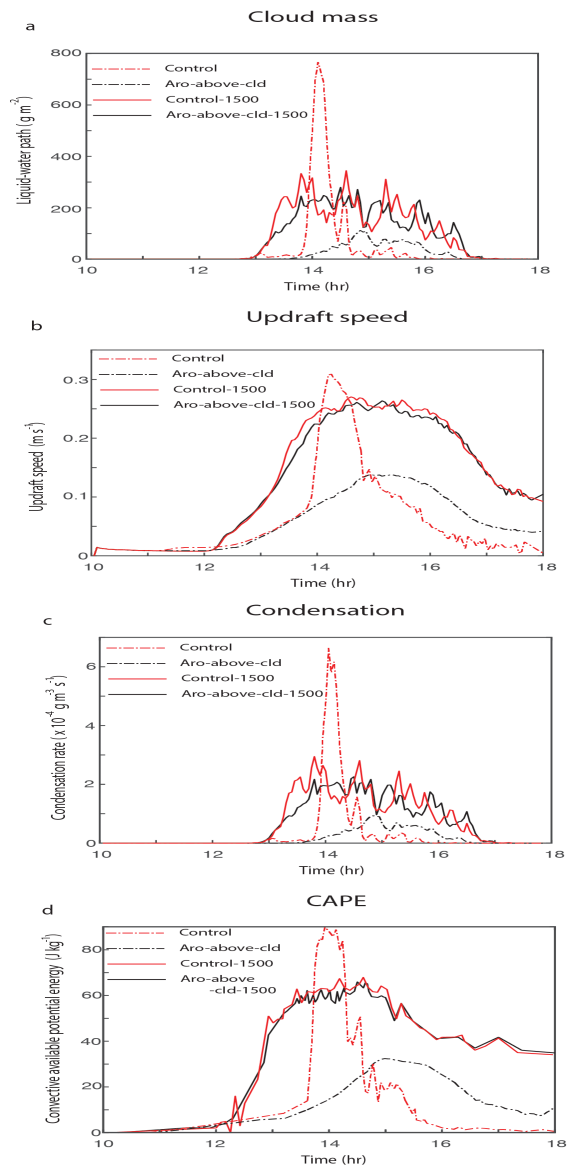
Figure 6



1089
1090
1091
1092
1093
1094
1095
1096

Figure 7

Deleted: 6



1098

1099

Figure 8

Deleted: 7

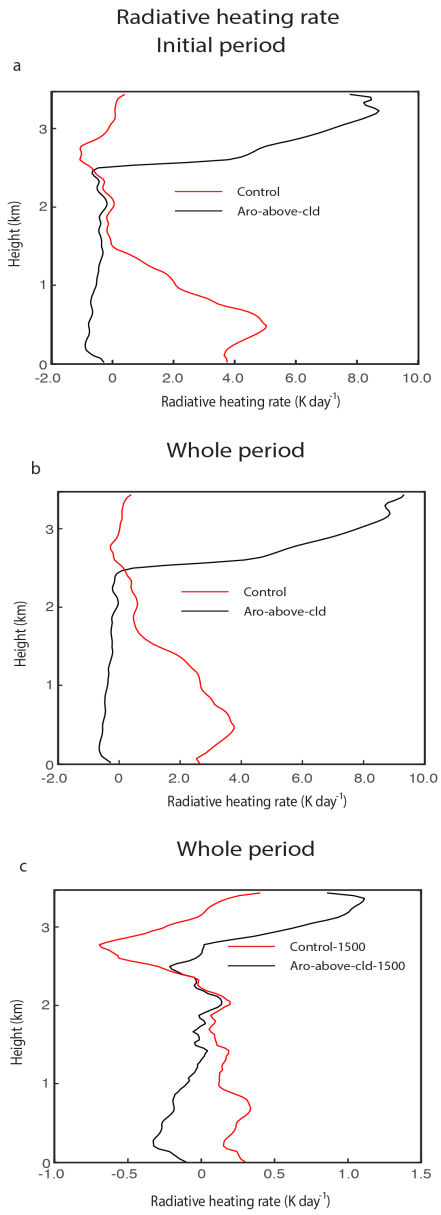


Figure 9

Deleted: 8

1101
1102
1103

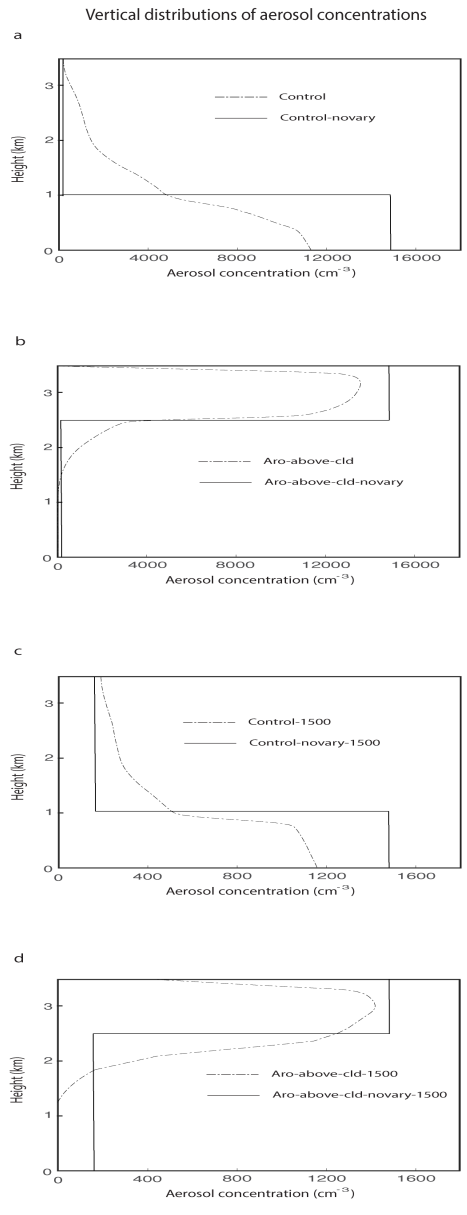
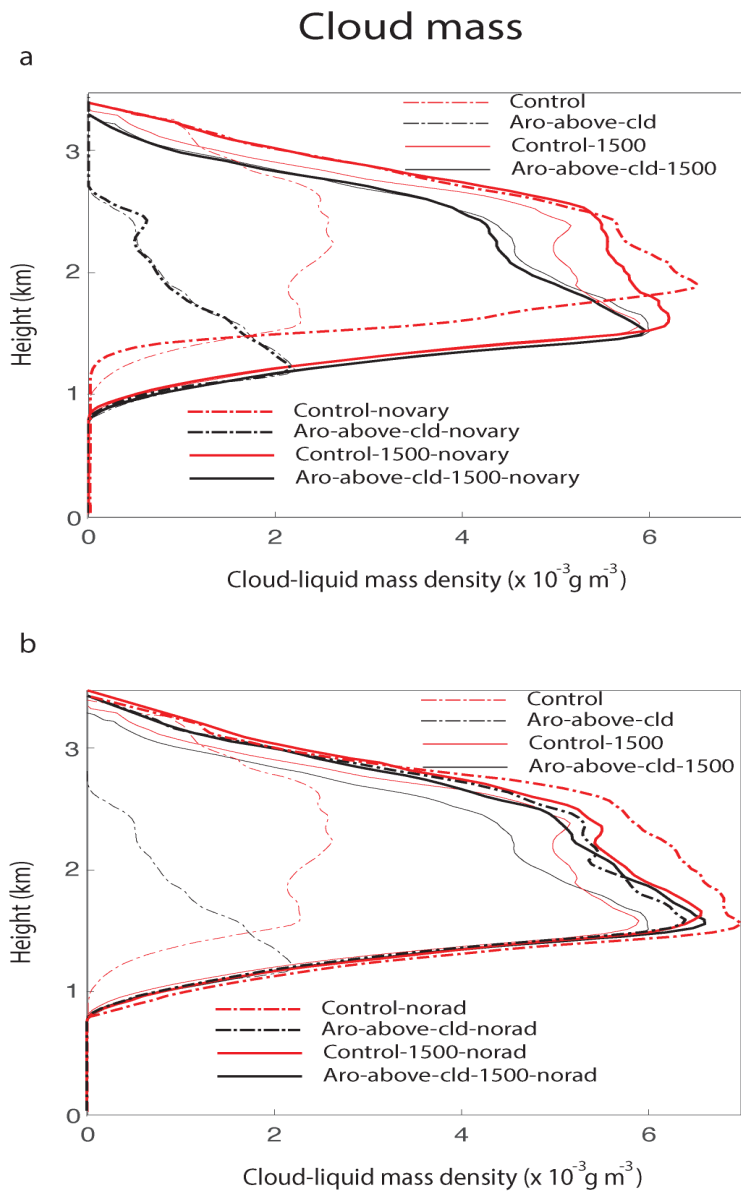


Figure 10

Deleted: 9

1105
1106
1107



1109
1110
1111

Figure 11

Deleted: 0